sensors

MDPI

Article

An Efficient Electrochemical Sensor Driven by Hierarchical Hetero-Nanostructures Consisting of RuO_2 Nanorods on WO_3 Nanofibers for Detecting Biologically Relevant Molecules

Hyerim Lee †, Yeomin Kim †, Areum Yu, Dasol Jin, Ara Jo, Youngmi Lee *, Myung Hwa Kim * and Chongmok Lee *

Department of Chemistry & Nanoscience, Ewha Womans University, Seoul 03760, Korea

* Correspondence: youngmilee@ewha.ac.kr (Y.L.); myungkim@ewha.ac.kr (M.H.K.); cmlee@ewha.ac.kr (C.L.); Tel.: +82-2-3277-6652 (Y.L.); +82-2-3277-4131 (M.H.K.); +82-2-3277-2344 (C.L.)

† Authors contribute this work equally.

Received: 26 June 2019; Accepted: 23 July 2019; Published: 26 July 2019

Abstract: By means of electrospinning with the thermal annealing process, we investigate a highly efficient sensing platform driven by a hierarchical hetero-nanostructure for the sensitive detection of biologically relevant molecules, consisting of single crystalline ruthenium dioxide nanorods (RuO_2 NRs) directly grown on the surface of electrospun tungsten trioxide nanofibers (WO_3 NFs). Electrochemical measurements reveal the enhanced electron transfer kinetics at the prepared RuO_2 NRs-WO_3 NFs hetero-nanostructures due to the incorporation of conductive RuO_2 NRs nanostructures with a high surface area, resulting in improved relevant electrochemical sensing performances for detecting H_2O_2 and L-ascorbic acid with high sensitivity.

Keywords: ruthenium dioxide; tungsten trioxide; nanofibers; nanorods; electrochemical sensors

1. Introduction

Recently, a variety of metal oxide nanostructures have been extensively utilized as efficient electrode substances owing to their outstanding electrocatalytic properties. Among them, ruthenium dioxide (RuO_2) has been well described as one of the best electrocatalysts for diverse energy related applications, such as the hydrogen evolution reaction (HER), oxygen evolution reaction (OER), and supercapacitors because of its high electric conductivity, catalytic activity, and thermal stability [1–3]. Especially, RuO_2 has been used as an efficient electrode system for supercapacitors owing to its excellent charging-discharging behavior [1,4–8]. Generally, RuO_2 as a promising catalytic material is often used in the forms of hybrid structures or alloys with other abundant transition metals in consideration of the relatively high cost of RuO_2. Thus, there have been previous reports regarding the use of RuO_2 nanostructures with other metal oxides as supercapacitors [9–12], and biosensing applications [1–3,13,14].

Tungsten trioxide (WO_3) nanostructures have been also extensively studied in various applications due to its earth-abundance, high durability, and chemical stabilities in aqueous acid media, as well as good electrochemical conductivity [15–18]. Thereby it has been developed as a catalyst for the hydrogen evolution reaction (HER) and supercapacitors in an acidic solution [19–22]. WO_3 also constitutes composites with other novel metals like Pt [23–26], Ir [17,23,27], and Ru [16,28–30], or supporting materials.

Nanostructured catalysts are applied to nonenzymatic electrochemical biosensors. Electrochemical properties can be enhanced from the increase of active surfaces. The detection of hydrogen peroxide (H_2O_2) is important in not only biomedical and environmental applications, but also in the enzymatic

system [31]. While ascorbic acid (AA) has an important role in the physiological function of organisms, a deficiency of AA causes several diseases [32,33]. Therefore, the detection and accurate quantification of target material with selectivity is highly required.

In this study, we introduce a facile fabrication of hybrid nanostructures consisting of single crystalline RuO_2 nanorods on eletrospun WO_3 nanofibers by utilizing electrospinning and thermal annealing processes. In addition, the fundamental electrochemical performances of RuO_2 nanorods-WO_3 nanofibers (RuO_2 NRs-WO_3 NFs) are carefully investigated, which confirm their characteristics of fast electron-transfer reactions and possibility as a catalytic sensing platform for detecting L-ascorbic acid (AA) and hydrogen peroxide (H_2O_2) in phosphate buffered solution (PBS).

2. Materials and Methods

Tungsten chloride (WCl_6, ≥ 99.9% true metal basis), ruthenium chloride hydrate ($RuCl_3 \cdot xH_2O$, 99.98% trace metal basis), poly(vinyl pyrrolidone) (PVP, MW = 1,300,000), N,N-dimethylformamide (DMF), potassium ferricyanide ($K_3[Fe(CN)_6]$), L-ascorbic acid (AA), 4-acetamidophenol (AP), dopamine hydrochloride (DA), uric acid (UA), D-(+)-glucose, hydrogen peroxide (H_2O_2, 35 wt% solution in water), sodium phosphate monobasic, and sodium phosphate dibasic were supplied by Sigma Aldrich (St. Louis, MO). Commercial Pt/C and Ir/C (both of them were 20 wt% each metal loading on Vulcan XC-72) were obtained from E-TEK Company. Sulfuric acid (H_2SO_4) and acetic acid were provided by Ducksan (Korea). Sodium hydroxide (NaOH) was purchased from Daejung (Korea). Deionized water with resistivity ≥ 18 MΩ·cm was used in all processes.

First, WO_3 nanofibers were synthesized by electrospinning and thermal annealing process according to the reported method [23]. To prepare electrospinning solution, 1.5 g WCl_6 were dissolved in 10.549 mL DMF with 1.25 g PVP and 0.191 mL acetic acid. After being stirred overnight, the solution was loaded into syringe and applied to the needle of the electrospinning system (Nano NC ESR 200R2). The needle was connected to a voltage power supply (applied voltage = 17.5 kV) at a flow rate of 5 μL/min, and the distance from needle tip to aluminum plate to collect as spun NFs was 15 cm. The collected electrospun NFs were calcinated at 500 °C for 1 h under a mixed gas atmosphere of 80 sccm of He and 10 sccm of O_2 with ramping rate of 1 °C/min.

Ruthenium hydroxide ($Ru(OH)_3$) precursor was prepared by a precipitation process via the acid-base reaction with controlling pH of aqueous solution. The pH of the final precursor solution at about pH 10 was carefully achieved by slowly dropping 0.1 M NaOH dilute solution into 5 mM $RuCl_3 \cdot xH_2O$ aqueous solution [2,13]. After precipitation, the precursor solution was washed five times with deionized water, and then re-dispersed in 2~3 mL pure deionized water again. To grow RuO_2 NRs on WO_3 NFs, 2 mg of WO_3 NFs was dispersed into 1 mL deionized water and then mixed with 1 mL $Ru(OH)_3$ precursor solution. After sonication for 30 min, the mixed solution was directly dropped on the center of Si wafer. WO_3 nanofibers containing $Ru(OH)_3$ precursors loaded on the Si wafer was placed into the center of a furnace and calcined at 300 °C for 5 h in air. The furnace was then allowed to cool to room temperature.

The surface morphology of as-grown products was examined by field emission scanning electron microscopy (FE-SEM; JEOL JSM-6700F). The detailed crystal structures were also investigated by a high-resolution transmission electron microscopy (HRTEM, Cs-corrected STEM, JEOL JEM-2100F) instrument equipped with selected area electron diffraction (SAED) micrographs and elemental EDX mapping with a Tecnai-F20 system operated at 200 kV. Additionally, high resolution X-ray diffraction measurement (XRD; Bruker D8 DISCOVER, Cu Kα radiation), and X-ray photoelectron spectroscopy (XPS; Theta Probe AR-XPS System. Al Kα radiation) were performed to investigate the crystal structure and surface binding energies of as-grown RuO_2 NR-WO_3 NFs.

For electrochemical measurements, a three-electrode system was used with a modified glassy carbon (GC) electrode (3 mm in diameter), a saturated calomel electrode (S.C.E.), and a coiled Pt wire (1 mm in diameter, length immersed in a solution ~ 10 cm) as the working electrode, the reference electrode, and the counter electrode, respectively. All electrochemical experiments conducted with

CHI 650E workstation (CH Instruments) and BAS100B (BAS Inc.). To modify the surface of a GC electrode with synthesized nanomaterials, 2 mg of RuO_2 NR-WO_3 NFs was suspended in 1.0 mL deionized water. Subsequently, 10 µL of the solution were dropped onto the GC electrode surface three times. Then, 10 µL of 0.05 wt% Nafion solution were loaded onto the modified GC electrode surface. Cyclic voltammetry (CV) measurements was used for analyze the capacitive behavior in 1 M H_2SO_4. For sensing experiments, linear sweep voltammetry (LSV) was also used with rotating disk electrode (RDE) at a scan rate of 5 mV s^{-1} with rotating speed of 1600 rpm, and amperometry measurements were used in 0.1 M phosphate buffered saline (PBS) at physiological condition pH (7.4).

3. Results and Discussion

3.1. Synthesis of Hybrid Nanostructures of RuO_2 Nanorods on Electrospun WO_3 Nanofibers

Figure 1A,B show FE-SEM images of WO_3 NFs annealed at 500 °C. The calcined WO_3 NFs revealed a very fine structure and the diameter of the fibers was around 200 nm. On the other hand, after the heat treatment of the mixed solution composed of $Ru(OH)_3$ precursors and WO_3 NFs at 300 °C for 5 h, it is readily identified that RuO_2 NRs were directly grown on the electrospun WO_3 NFs as shown in Figure 1C,D. Figure 1D represents the as grown RuO_2 NRs covering the entire surface of WO_3 NFs. The lateral dimension of RuO_2 NRs is estimated to be about 40 nm and the length up to 300 nm. Careful EDS measurements indicate that the atomic ratio of Ru to W is confirmed as 45:55. According to our previous real-time study by in situ synchrotron XRD, a simple recrystallization process by thermal annealing might be responsible for the growth mechanism of RuO_2 NRs. It was carefully suggested that Ru diffusion to the amorphous nanoparticles followed by diffusion to the growing surface of the nanorod plays an essential role in the growth of RuO_2 NRs in oxygen ambient, which is supported by the nucleation theory [34].

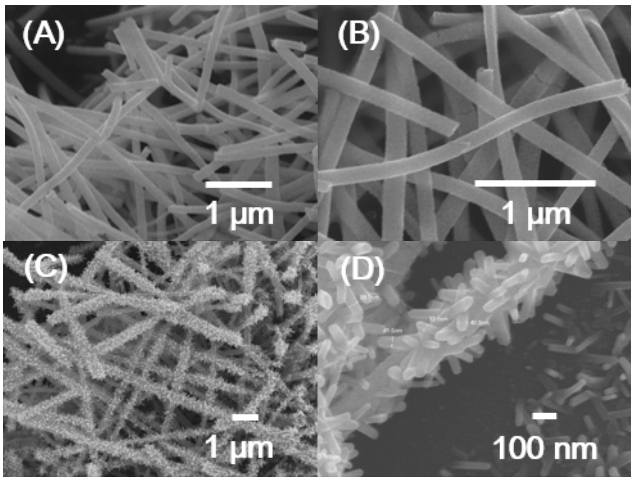

Figure 1. (**A**,**B**) SEM images of pure electrospun WO_3 nanofibers (WO_3 NFs). (**C**,**D**) SEM images of as grown RuO_2 nanorods on the electrospun WO_3 nanofibers (RuO_2 NRs-WO_3 NFs).

Figure 2 represents XRD spectra and high resolution XPS spectra of composite RuO_2 NRs-WO_3 NFs and pure WO_3 NFs. XRD spectrum of pure WO_3 NFs in Figure 2B demonstrates that all peaks are closely matched with the monoclinic phase of WO_3 [19,35]. On the other hand, XRD spectrum of composite RuO_2 NR-WO_3 NFs confirms the same monoclinic phase WO_3 peaks including two major peaks at 27.1° and 34.8° corresponding to (110) and (101) crystallographic planes of tetragonal RuO_2 structure as displayed in Figure 2A [2,13]. To investigate the oxidation states of Ru, W, and O atoms, XPS measurements were performed. In Figure 2C, two separated binding energies at 35.1 eV and 37.3 eV are clearly identified as two spin-orbit states of W $4f_{5/2}$ and W $4f_{7/2}$, respectively, which indicates the oxidation state of +6 for W in WO_3 NFs [16,36]. Both high resolution Ru 3d and Ru

3p spectra were shown in Figure 2E,F. Although the peak position of Ru $3d_{3/2}$ is overlapped with C 1s [16,37], the oxidation state of Ru species is readily identified to Ru^{4+} based on the binding energies of 280.7 eV and 462.8 eV, indexed to Ru $3d_{5/2}$ and Ru $3p_{3/2}$, respectively [37,38]. In addition, the peak at 530.5 eV of O 1s is associated with O^{2-} in RuO_2 and WO_3 metal oxides as shown in Figure 2D.

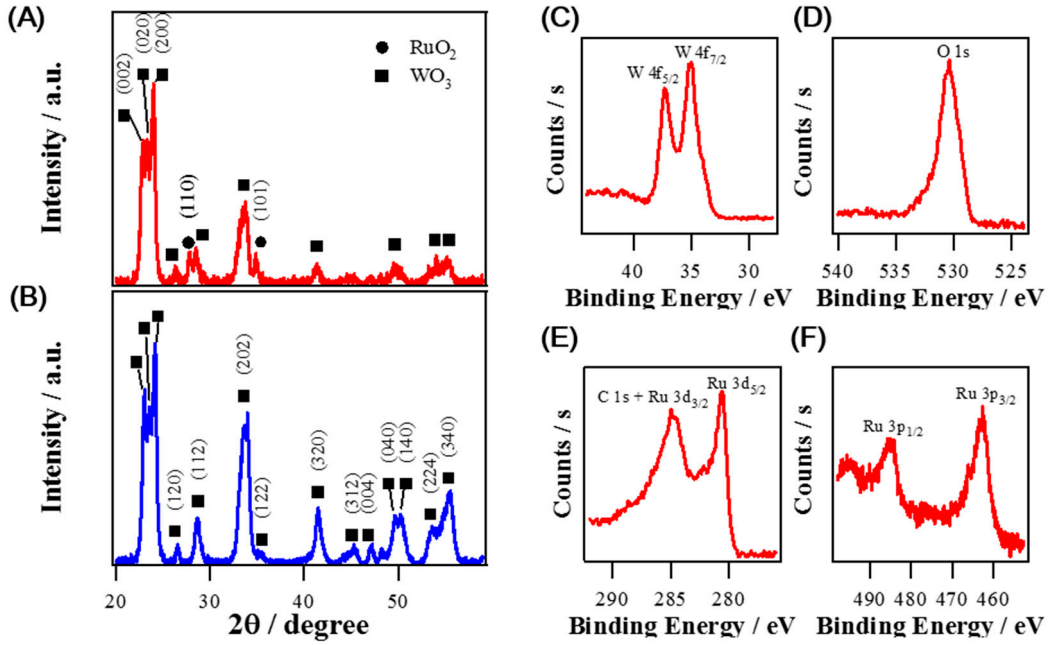

Figure 2. (**A**) XRD spectrum for RuO_2 NRs-WO_3 NFs (**B**) XRD spectrum for pure WO_3 NFs. (**C**–**F**) high resolution XPS spectra for RuO_2 NRs-WO_3 NFs, (**C**) W 4f, (**D**) O 1s, (**E**) Ru 3d, and (**F**) Ru 3p regions, respectively.

Figure 3 indicates TEM images and SAED pattern for a single WO_3 nanofiber covered with RuO_2 nanorods. As shown in Figure 3A,B, low-magnification TEM images show the high density of RuO_2 nanorods directly grown on the porous surface of WO_3 nanofiber. The SAED pattern shown in Figure 3E reveals the existence of many different crystalline phases in a WO_3 nanofiber which confirms the polycrystalline nature of a WO_3 nanofiber. On the contrary, the fast Fourier transform (FFT) of the lattice-resolved image for a RuO_2 nanorod in Figure 3F represents highly ordered lattice fringes with a single crystal nature. The values of lattice spacing of adjacent planes are estimated by about 0.318 nm and 0.263 nm, corresponding to those of between the (110) planes and (101) for the tetragonal RuO_2, respectively. Furthermore, TEM-EDS element mapping analysis from the high-angle annular dark field (HAADF) STEM image shown in Figure S1 confirms the homogenous distribution of Ru, W, and O in distinct regions in the hierarchical nanostructure. W atoms exist on the backbone of the nanofibers, whereas Ru atoms exclusively exist on the branched nanorods. Oxygen atoms exist both on the backbone of the nanofibers and branched nanorods. Thus, we successfully fabricate the high density of single-crystalline RuO_2 nanorods on WO_3 nanofibers by using a combination of an electrospinning process and a thermal annealing process. Our growth process thus provides a simple methodology for the fabrication of highly efficient electrocatalysts.

3.2. *Electrochemical Properties for Capacitive Behaviors of RuO_2 NRs-WO_3 NFs*

The general electrochemical activities of RuO_2 NRs-WO_3 NFs and WO_3 NFs were examined by CV in 10 mM $[Fe(CN)_6]^{3-}$ aqueous solution containing 1 M KCl. Figure S2 displays CV curves of RuO_2 NRs-WO_3 NFs and WO_3 NFs at a scan rate 100 mV s^{-1}. Voltammetric current peaks at RuO_2 NRs-WO_3 NFs are reversible, while those of WO_3 NFs are quasi-reversible. It seems to be ascribed to that RuO_2 NRs-WO_3 NFs allow very facile heterogeneous electron transfer kinetics with high electric

conductivities in contrast to WO_3 NFs. Moreover, RuO_2 NRs-WO_3 NFs show a much larger charging current in CV than WO_3 NFs.

To characterize the charging behavior of the synthesized materials, CV was measured for a potential range from 0.1 V to 0.9 V (vs. S.C.E.) in 1 M H_2SO_4 as seen in Figure 4. Figure 4A shows CV results comparing RuO_2 NRs-WO_3 NFs and WO_3 NFs at a scan rate 100 mV s^{-1}. It supports the enhanced capacity of RuO_2 NRs-WO_3 NFs as the RuO_2 NRs were grown on WO_3 NFs. To examine the charging performance, the average specific capacitance values (C_{sp}, F g^{-1}) were calculated with the following Equation (1) using CV curves shown in Figure 4B.

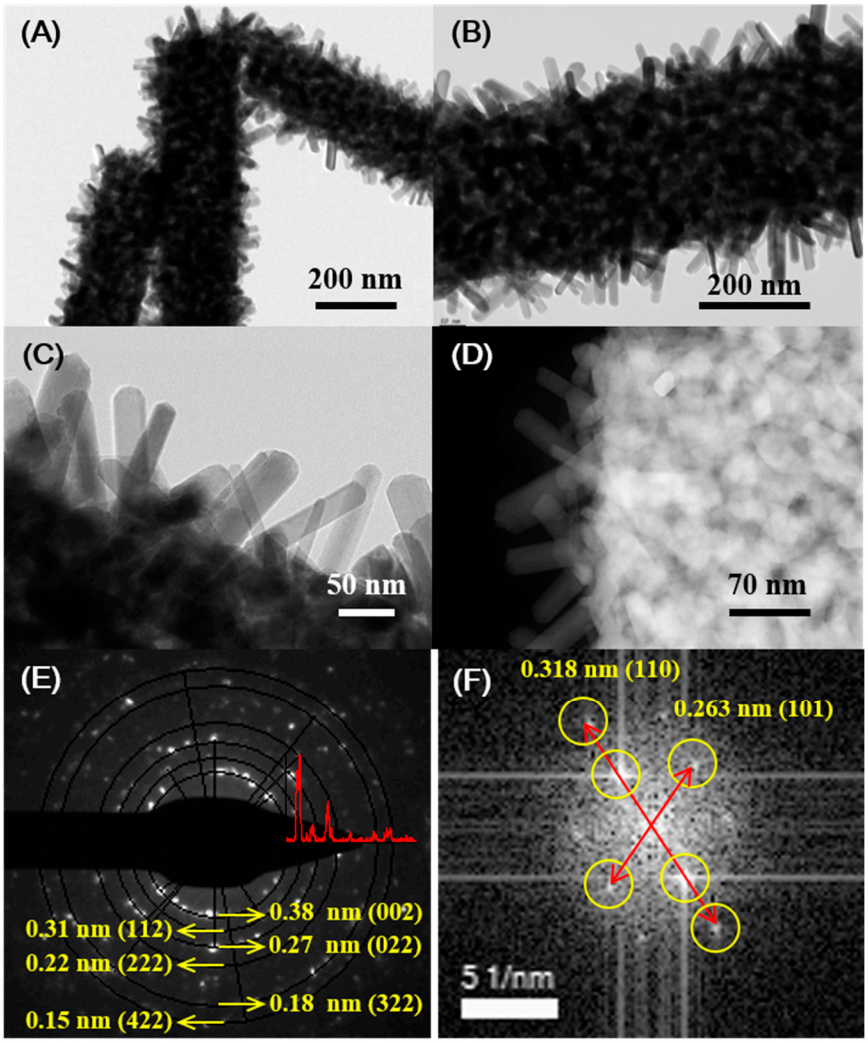

Figure 3. (**A**,**B**) low magnification TEM images for RuO_2 nanorods on a single WO_3 nanofiber. (**C**) The high resolution TEM image for RuO_2 nanorods on a single WO_3 nanofiber. (**D**) The bright field TEM image for RuO_2 nanorods on a single WO_3 nanofiber. (**E**,**F**) SAED pattern for a WO_3 nanofiber and fast Fourier transform (FFT) of the lattice-resolved image for a single RuO_2 nanorod.

$$C_{sp} = \frac{1}{2 \times v \times \Delta m \times \Delta V} \int IdV \quad (1)$$

where v is the scan rate (V s^{-1}), Δm is the weight of electrode materials, ΔV is the potential range, and IdV is the area under CV curve [39]. At the scan rate of 10 mV s^{-1}, the C_{sp} values of the synthesized materials, RuO_2 NRs-WO_3 NFs and WO_3 NFs, are 98.15 F g^{-1} and 0.95 F g^{-1}, respectively. The C_{sp} of RuO_2 NRs-WO_3 NFs is obviously 103-fold higher than that of WO_3 NFs as shown in Figure 4C.

As the scan rate increases, C_{sp} becomes smaller and the C_{sp} of RuO_2 NRs-WO_3 NFs and WO_3 NFs decreased down to 57% and 42%, respectively, while increasing the scan rate from 10 mV s^{-1} to 200 mV s^{-1}. This additionally indicates the successful decoration of WO_3 NFs with RuO_2 NRs forming the hierarchical hetero-nanostructures.

Electrochemical impedance spectroscopy (EIS) was also employed to examine the electrochemical behavior of RuO_2 NRs-WO_3 NFs and WO_3 NFs. EIS measurement was carried out at 0.5 V (vs. S.C.E.) under the same condition of CV experiments with a frequency range of 0.1 Hz–1000 kHz as shown in Figure S3. The Nyquist plot of RuO_2 NRs-WO_3 NFs was closer to a vertical line than that of WO_3 NFs, exhibiting nearly pure capacitive behavior of RuO_2 NR-WO_3 NFs [1,40]. The stability of RuO_2 NRs-WO_3 NFs for capacitance was demonstrated by monitoring the change of C_{sp} during repeated CV cycles as depicted in Figure 4D. RuO_2 NRs-WO_3 NFs excellently maintained about 96% of its original C_{sp} for the 1000 CV cycles at a scan rate of 100 mV s^{-1}.

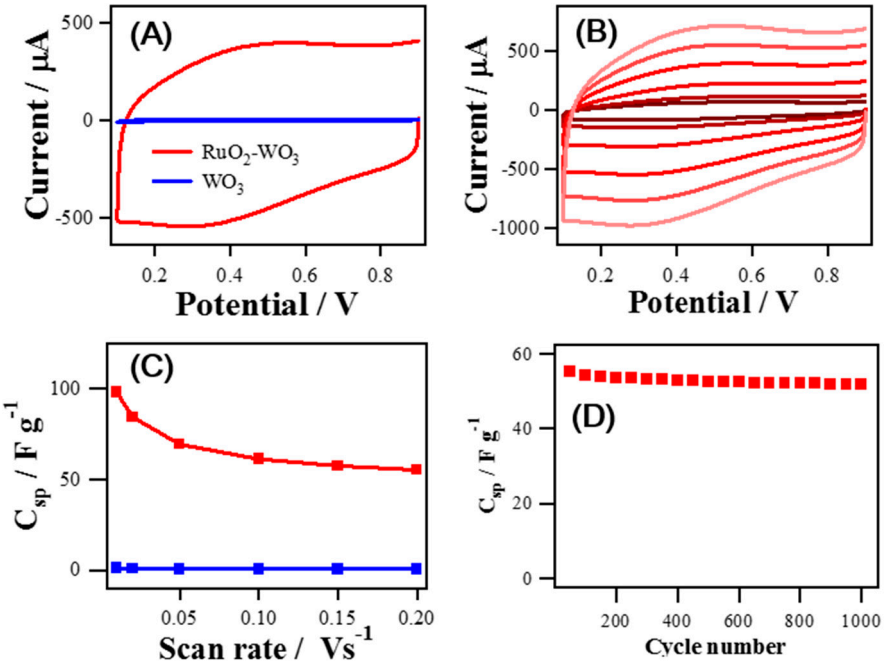

Figure 4. Capacitive current measurements in 1 M H_2SO_4 solution for (**A**) RuO_2 NRs-WO_3 NFs and WO_3 NFs at a scan rate 100 mV s^{-1}, and (**B**) RuO_2 NRs-WO_3 NFs with varing the scan rate from 10 mV s^{-1} to 200 mV s^{-1}. (**C**) Changes of specific capacitance (C_{sp}) values of RuO_2 NRs-WO_3 NFs and WO_3 NFs as a function of the CV scan rate (from 10 mV s^{-1} to 200 mV s^{-1}). (**D**) Plot of the C_{sp} values of RuO_2 NRs-WO_3 NFs depending on the number of repeated CV cycles in 1 M H_2SO_4.

3.3. Applications to Electrochemical Sensing of AA and H_2O_2

The electrochemical properties of RuO_2 NRs-WO_3 NFs for AA oxidation were also studied. LSV measurements in 0.1 M PBS were used for examining the oxidations of various biomaterials such as AA, DA, UA, AP, and glucose. The chosen concentrations are slightly above the physiological concentrations. As shown in Figure 5A, AA oxidation started to occur from the most negative potential compared with other biomaterials. Amperometric measurements of RuO_2 NRs-WO_3 NFs and WO_3 NFs were conducted at 0 V (vs. S.C.E.) which possibly allow for the oxidation of AA only, excepting for the other tested biomolecules as seen in the LSV results of Figure 5A.

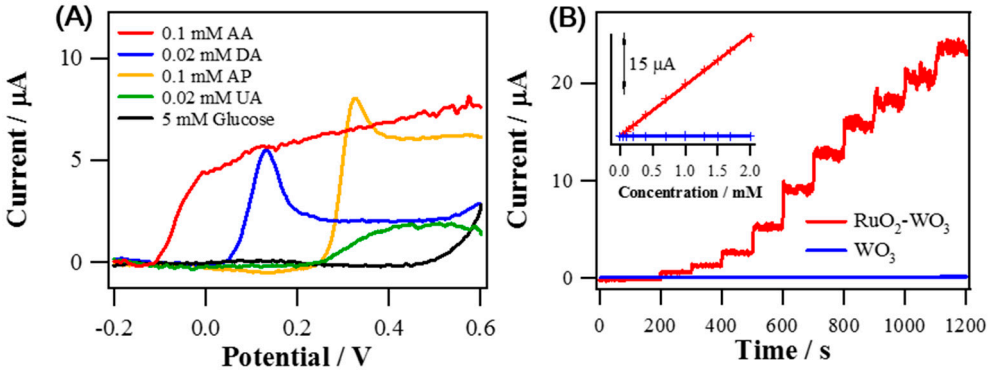

Figure 5. (**A**) Background-corrected LSVs of RuO_2 NRs-WO_3 NFs obtained in 0.1 M PBS (pH 7.4) independently containing one of 0.1 mM AA, 0.02 mM DA, 0.1 mM AP, 0.02 mM UA, 5 mM glucose (scan rate of 5 mV s^{-1}; and rotating speed of 1600 rpm). (**B**) Amperometric current responses of RuO_2 NRs-WO_3 NFs and WO_3 NFs for successive AA standard solution injections to increase the AA bulk concentration from 5 μM to 2 mM in 0.1 M PBS (pH 7.4) with E_{app} = 0 V (vs. S.C.E.). The inset: The calibration curves showing the current responses vs. concentration.

As observed in Figure 5B, the anodic currents of both electrodes were increased linearly with the concentration of AA increased from 5 μM to 2 mM. Also, the calibration curves based on the amperometric data were depicted in inset of Figure 5B. The sensitivity of RuO_2 NRs-WO_3 NFs (171.7 μA mM^{-1} cm^{-2}, R^2 = 0.9990, normalized to GC substrate electrode area, 0.072 cm^2) were surprisingly increased by 244 times compared to that of WO_3 NFs (0.704 μA mM^{-1} cm^{-2}, R^2 = 0.9990). Most of the typical biological samples are complex, having various oxidizable species, so selectivity to a targeted analyte is an essential requirement for any sensor. In Figure 6A, current responses for AA oxidation were stable against the additions of 0.1 mM AP, 0.1 mM UA, 0.1 μM DA and 5 mM glucose at 0 V. Additionally, the stability of RuO_2 NRs-WO_3 NFs was measured by monitoring the change of current at 0 V in 0.1 M PBS containing 0.3 mM AA. The amperometric response of RuO_2 NRs-WO_3 NFs retained 96% of the initial current level during over a 4200-s measurement in Figure 6B, supporting its excellent stability. Table 1 summarizes the properties of RuO_2 NRs-WO_3 NFs in comparison with other Ru-based materials used as AA sensors.

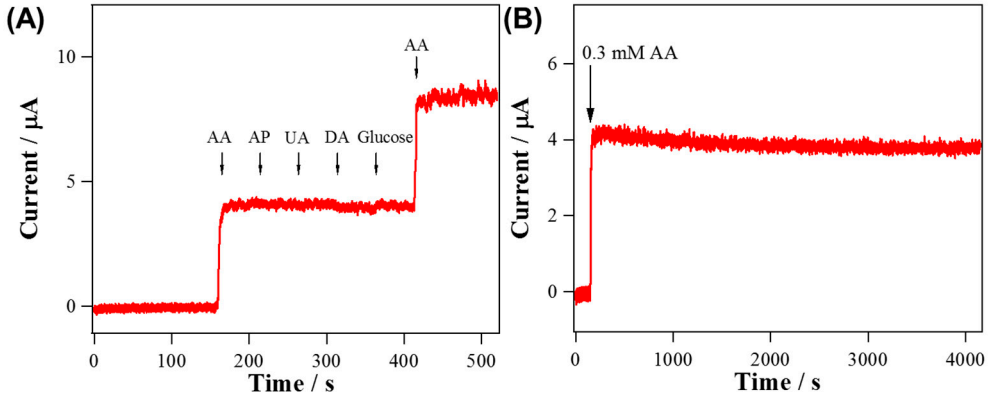

Figure 6. (**A**) Amperometric response of RuO_2 NRs-WO_3 NFs to sequential additions of 0.3 mM AA, 0.1 mM AP, 0.1 mM UA, 0.1 μM DA, 5 mM glucose and 0.6 mM AA to 0.1 M PBS (pH 7.4) with E_{app} = 0 V (vs. S.C.E.). (**B**) Continuous amperometric response of RuO_2 NRs-WO_3 NFs to 0.3 mM AA in 0.1 M PBS during 4200 s with E_{app} = 0 V (vs. S.C.E.).

Table 1. Comparison of the analytical performances of previous reported Ru-based AA sensors.

Electrodes	Methods	Solutions	Potential /V	Sensitivity /μAmM^{-1} cm^2	Linear Range /μM
RuO_2 NRs-WO_3 NFs [1]	Amperometry	PBS (pH 7.4)	0	171.7	5–2000
RuO_2-Co_3O_4 hybrid nanotubes [2]	Amperometry	PBS (pH 7.4)	0.05	204	~500
RuO_2NWs-TiO_2NFs [3]	Amperometry	PBS (pH 7.4)	0.018	268.2	10–1500
hAu-Ru nanoshells [4]	Amperometry	PBS (pH 7.4)	0.05	426	5–2000
AC-RuON-GCE [5]	DPV	PBS (pH 7.0)	−0.053	85.9	47–181.8
Screen-printing RuO_2 [6]	Amperometry	PBS (pH 7.4)	0.058	2.79	0–4000

[1] This work, [2] Ref. [3], [3] Ref. [13], [4] Ref. [41], [5] Ref. [42], [6] Ref, [43].

The catalytic effect of RuO_2 NRs-WO_3 NFs for H_2O_2 reduction was also measured. Figure 7A shows overlaid LSV results of RuO_2 NRs-WO_3 NFs and WO_3 NFs. It presents clearly that H_2O_2 reduction at RuO_2 NRs-WO_3 NFs starts from a much less negative potential with much greater reduction current level than that at WO_3 NFs. In fact, the cathodic current level measured at −0.2 V (vs. S.C.E.) was more greatly increased for RuO_2 NRs-WO_3 NFs than WO_3 NFs in response to the successive increase of H_2O_2 concentration (Figure 7B). Inset of Figure 7B shows the calibrated current vs concentration with good linearity. Obtained sensitivities from the calibration curves are 619.7 μA mM^{-1} cm^{-2} (R^2 = 0.9960), and 5.5 μA mM^{-1} cm^{-2} (R^2 = 0.9384) for RuO_2 NRs-WO_3 NFs and WO_3 NFs, respectively. Sensitivity of RuO_2 NR-WO_3 NFs is 112-fold higher than the value of WO_3 NFs, and therefore it supports the enhanced activities of RuO_2 NRs-WO_3 NFs toward H_2O_2 reduction. The H_2O_2 reduction current instead of the oxidation current was monitored to sense H_2O_2 in order to avoid the interference from many oxidizable species generally present in biological systems. Figure S4 represents the selectivity of RuO_2 NRs-WO_3 NFs for H_2O_2 reduction. The current responses of RuO_2 NRs-WO_3 NFs at −0.2 V (vs. S.C.E.) for H_2O_2 reduction were obvious; however, there were no noticeable responses to the successive injections of other biological materials: 0.1 mM AA, 0.1 mM UA, 0.1 μM DA, 5 mM glucose, 0.1 mM AP, and 30 μM O_2. RuO_2 NR-WO_3 NFs show relatively excellent catalytic activities for H_2O_2 reduction compared to other previous Ru-based materials as compared in Table 2. RuO_2 NRs-WO_3 NFs for measuring H_2O_2 reduction current was less stable than that for AA oxidation. In fact, H_2O_2 reduction current measured at −0.2 V was decreased to ~60% of the initial current level after 4200-s continuous measurement (data not shown).

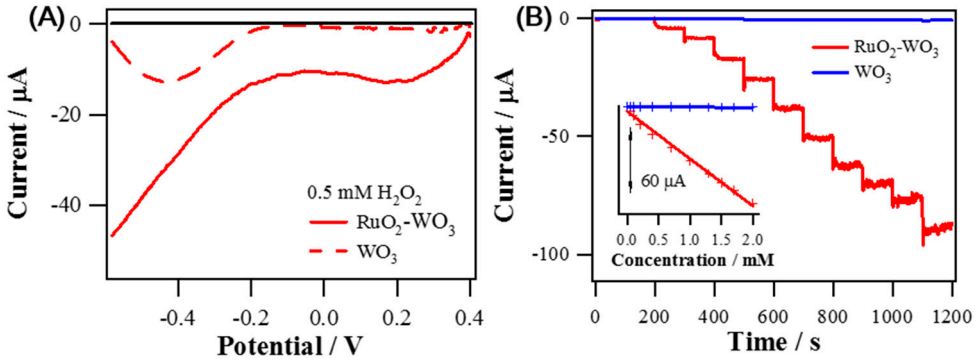

Figure 7. (**A**) Background-corrected LSVs of RuO_2 NRs-WO_3 NFs and WO_3 NFs obtained in 0.1 M PBS (pH 7.4) containing 0.5 mM H_2O_2 with a scan rate of 5 mV s^{-1}, at an electrode rotating speed of 1600 rpm. (**B**) Amperometric current responses of RuO_2 NRs-WO_3 NFs and WO_3 NFs to successive H_2O_2 injections from 0.005 mM to 2 mM in 0.1 M PBS (pH 7.4) at −0.2 V (vs. S.C.E.); the inset: corresponding calibration curves.

Table 2. Summary of the analytical performances of reported Ru-based H_2O_2 sensors.

Electrodes	Methods	Solutions	Potential /V	Sensitivity /μA mM^{-1} cm^{-2}	Linear Range /μM
RuO_2 NRs-WO_3 NFs [1]	Amperometry	0.1 M PBS	−0.2	619.7	5–2000
RuO_2-ReO_3 (0.11) [2]	Amperometry	0.1 M PBS	−0.2	667.8	0–5000
RuO_2NNs-TiO_2 NRs [3]	Amperometry	0.05M PBS	0	53.8	1–1000
RuO_2 NWs-Rh_2O_3 NF [4]	Amperometry	0.05 M PBS	0.12	283.1	0–1000
HRP/Chi-GAD/RuNPs [5]	Amperometry	Saturated PBS	−0.3	0.798	5090–15,000
Nafion-RuO_2-AuNP flim [6]	Amperometry	PBS	−0.4	15.44	0.001–30,000

[1] This work, [2] Ref. [1], [3] Ref. [2], [4] Ref. [14], [5] Ref. [44], [6] Ref, [45]. HRP: horseradish peroxidase, Chi: chitosan, GAD: glutaraldehyde

4. Conclusions

We report the successful fabrication of single crystalline RuO_2 nanorods on WO_3 nanofibers by electrospinning and calcination. Microscopic and spectroscopic measurements such as SEM with EDS, XRD, and XPS were used to characterize the structure and composition of RuO_2 NRs-WO_3 NFs. The RuO_2 NRs-WO_3 NFs showed improved electrocatalytic activities over WO_3 NFs through a series of electrochemical measurements. In 1 M H_2SO_4 solution, RuO_2 NRs-WO_3 NFs represent a higher C_{sp}, 98.15 F g^{-1}, by 103-fold with good stability and a sharper slope than pure WO_3 NFs. Additionally, the RuO_2 NRs-WO_3 NFs have dramatically enhanced sensing abilities, in accordance with 224 times (171.7 μA mM^{-1} cm^{-2}) sensitivity for AA oxidation, and 112 times (619.7 μA mM^{-1} cm^{-2}) sensitivity for H_2O_2 reduction, respectively, compared to those of pure WO_3 NFs. These results thus suggest that RuO_2 NRs-WO_3 NFs could be a promising candidate electrocatalyst for the fabrication of an efficient electrochemical sensor due to its highly effective electrochemical performance.

Supplementary Materials: The followings are available online at http://www.mdpi.com/1424-8220/19/15/3295/s1, Figure S1: EDS elemental mappings, Figure S2: Cyclic voltammograms, Figure S3: Nyquist plots, Figure S4: Amperometric response.

Author Contributions: Authors contribute as conceptualization, C.L., Y.L. and M.H.K.; methodology, H.L., Y.K., D.J.; validation, H.L., A.Y. and D.J.; formal analysis, H.L. and Y.K.; investigation, A.J. and A.Y.; data curation, H.L. and A.Y.; writing—original draft preparation, C.L., Y.L. and M.H.K.; writing—review and editing, C.L., Y.L. and M.H.K.; supervision, C.L.; funding acquisition, C.L.,Y.L. and M.H.K.

Funding: This work was financially supported by Basic Science Research Program through the National Research Foundation of Korea (NRF) funded by the Ministry of Education (NRF-2018R1A6A1A03025340 for YL and 2016R1D1A1B03934962 for KMH) and by the National Research Foundation of Korea (NRF) funded by the Ministry of Science and ICT (NRF-2019R1F1A1059969 for CL).

Conflicts of Interest: The authors declare no conflict of interest.

References

1. Kim, Y.L.; Choi, H.-A.; Lee, N.-S.; Son, B.; Kim, H.J.; Baik, J.M.; Lee, Y.; Lee, C.; Kim, M.H. RuO_2–ReO_3 composite nanofibers for efficient electrocatalytic responses. *Phys. Chem. Chem. Phys.* **2015**, *17*, 7435–7442. [CrossRef] [PubMed]
2. Kim, S.-J.; Cho, Y.K.; Seok, J.; Lee, N.-S.; Son, B.; Lee, J.W.; Baik, J.M.; Lee, C.; Lee, Y.; Kim, M.H. Highly Branched RuO_2 Nanoneedles on Electrospun TiO_2 Nanofibers as an Efficient Electrocatalytic Platform. *ACS Appl. Mater. Interfaces* **2015**, *7*, 15321–15330. [CrossRef] [PubMed]
3. Jang, H.S.; Yang, Y.; Lee, N.-S.; Son, B.; Lee, Y.; Lee, C.; Kim, M.H. Electrospun RuO_2–Co_3O_4 hybrid nanotubes for enhanced electrocatalytic activity. *Mater. Lett.* **2015**, *139*, 405–408. [CrossRef]
4. Sugimoto, W.; Iwata, H.; Yokoshima, K.; Murakami, Y.; Takasu, Y. Proton and Electron Conductivity in Hydrous Ruthenium Oxides Evaluated by Electrochemical Impedance Spectroscopy: The Origin of Large Capacitance. *J. Phys. Chem. B* **2005**, *109*, 7330–7338. [CrossRef] [PubMed]
5. Hu, C.-C.; Chang, K.-H.; Lin, M.-C.; Wu, Y.-T. Design and Tailoring of the Nanotubular Arrayed Architecture of Hydrous RuO_2 for Next Generation Supercapacitors. *Nano Lett.* **2006**, *6*, 2690–2695. [CrossRef]
6. Zang, J.; Bao, S.-J.; Li, C.M.; Bian, H.; Cui, X.; Bao, Q.; Sun, C.Q.; Guo, J.; Lian, K. Well-Aligned Cone-Shaped Nanostructure of Polypyrrole/RuO_2 and Its Electrochemical Supercapacitor. *J. Phys. Chem. C* **2008**, *112*, 14843–14847. [CrossRef]
7. Xia, H.; Meng, Y.S.; Yuan, G.; Cui, C.; Lu, L. A Symmetric RuO_2/RuO_2 Supercapacitor Operating at 1.6 V by Using a Neutral Aqueous Electrolyte. *Electrochem. Solid-State Lett.* **2012**, *15*, A60–A63. [CrossRef]
8. Lee, J.-B.; Jeong, S.-Y.; Moon, W.-J.; Seong, T.-Y.; Ahn, H.-J. Preparation and characterization of electro-spun RuO_2–Ag_2O composite nanowires for electrochemical capacitors. *J. Alloys Compd.* **2011**, *509*, 4336–4340. [CrossRef]
9. Wang, Y.-G.; Zhang, X.-G. Preparation and electrochemical capacitance of RuO_2/TiO_2 nanotubes composites. *Electrochim. Acta* **2004**, *49*, 1957–1962.
10. Wang, Y.-G.; Wang, Z.-D.; Xia, Y.-Y. An asymmetric supercapacitor using RuO_2/TiO_2 nanotube composite and activated carbon electrodes. *Electrochim. Acta* **2005**, *50*, 5641–5646. [CrossRef]
11. Rack Ahn, Y.; Park, C.; Mu Jo, S.; Young Kim, D. Enhanced charge-discharge characteristics of RuO_2 supercapacitors on heat-treated TiO_2 nanorods. *Appl. Phys. Lett.* **2007**, *90*, 122106.
12. Lokhande, C.; Park, B.-O.; Park, H.-S.; Jung, K.-D.; Joo, O.-S. Electrodeposition of TiO_2 and RuO_2 thin films for morphology-dependent applications. *Ultramicroscopy* **2005**, *105*, 267–274. [CrossRef]
13. Kim, S.-J.; Cho, Y.K.; Lee, C.; Kim, M.H.; Lee, Y. Real-time direct electrochemical sensing of ascorbic acid over rat liver tissues using RuO_2 nanowires on electrospun TiO_2 nanofibers. *Biosens. Bioelectron.* **2016**, *77*, 1144–1152. [CrossRef] [PubMed]
14. Kim, Y.L.; Ha, Y.; Lee, N.-S.; Kim, J.G.; Baik, J.M.; Lee, C.; Yoon, K.; Lee, Y.; Kim, M.H. Hybrid architecture of rhodium oxide nanofibers and ruthenium oxide nanowires for electrocatalysts. *J. Alloys Compd.* **2016**, *663*, 574–580. [CrossRef]
15. Huang, Z.-F.; Song, J.; Pan, L.; Zhang, X.; Wang, L.; Zou, J.-J. Tungsten Oxides for Photocatalysis, Electrochemistry, and Phototherapy. *Adv. Mater.* **2015**, *27*, 5309–5327. [CrossRef] [PubMed]
16. Janáky, C.; Chanmanee, W.; Rajeshwar, K. On the Substantially Improved Photoelectrochemical Properties of Nanoporous WO_3 Through Surface Decoration with RuO_2. *Electrocatalysis* **2013**, *4*, 382–389. [CrossRef]
17. Baruffaldi, C.; Cattarin, S.; Musiani, M. Deposition of non-stoichiometric tungsten oxides+MO_2 composites (M = Ru or Ir) and study of their catalytic properties in hydrogen or oxygen evolution reactions. *Electrochim. Acta* **2003**, *48*, 3921–3927. [CrossRef]
18. Zheng, H.; Ou, J.Z.; Strano, M.S.; Kaner, R.B.; Mitchell, A.; Kalantar-zadeh, K. Nanostructured Tungsten Oxide—Properties, Synthesis, and Applications. *Adv. Funct. Mater.* **2011**, *21*, 2175–2196. [CrossRef]
19. Zhou, X.; Qiu, Y.; Yu, J.; Yin, J.; Bai, X. High electrochemical activity from hybrid materials of electrospun tungsten oxide nanofibers and carbon black. *J. Mater. Sci.* **2012**, *47*, 6607–6613. [CrossRef]
20. Wei, H.; Ding, D.; Yan, X.; Guo, J.; Shao, L.; Chen, H.; Sun, L.; Colorado, H.A.; Wei, S.; Guo, Z. Tungsten Trioxide/Zinc Tungstate Bilayers: Electrochromic Behaviors, Energy Storage and Electron Transfer. *Electrochim. Acta* **2014**, *132*, 58–66. [CrossRef]

21. Yoon, S.; Kang, E.; Kim, J.K.; Lee, C.W.; Lee, J. Development of high-performance supercapacitor electrodes using novel ordered mesoporous tungsten oxide materials with high electrical conductivity. *Chem. Commun.* **2011**, *47*, 1021–1023. [CrossRef] [PubMed]
22. Shi, J.; Pu, Z.; Liu, Q.; Asiri, A.M.; Hu, J.; Sun, X. Tungsten nitride nanorods array grown on carbon cloth as an efficient hydrogen evolution cathode at all pH values. *Electrochim. Acta* **2015**, *154*, 345–351. [CrossRef]
23. Shin, J.; Choi, S.-J.; Youn, D.-Y.; Kim, I.-D. Exhaled VOCs sensing properties of WO_3 nanofibers functionalized by Pt and IrO_2 nanoparticles for diagnosis of diabetes and halitosis. *J. Electroceram.* **2012**, *29*, 106–116. [CrossRef]
24. Shim, J.; Lee, C.-R.; Lee, H.-K.; Lee, J.-S.; Cairns, E.J. Electrochemical characteristics of Pt–WO_3/C and Pt–TiO_2/C electrocatalysts in a polymer electrolyte fuel cell. *J. Power Sources* **2001**, *102*, 172–177. [CrossRef]
25. Jayaraman, S.; Jaramillo, T.F.; Baeck, S.-H.; McFarland, E.W. Synthesis and Characterization of Pt–WO_3 as Methanol Oxidation Catalysts for Fuel Cells. *J. Phys. Chem. B* **2005**, *109*, 22958–22966. [CrossRef] [PubMed]
26. Rajesh, B.; Karthik, V.; Karthikeyan, S.; Ravindranathan Thampi, K.; Bonard, J.M.; Viswanathan, B. Pt–WO_3 supported on carbon nanotubes as possible anodes for direct methanol fuel cells. *Fuel* **2002**, *81*, 2177–2190. [CrossRef]
27. Kuo, L.-M.; Chen, K.-N.; Chuang, Y.-L.; Chao, S. A Flexible pH-Sensing Structure Using WO_3/IrO_2 Junction with Al_2O_3 Encapsulation Layer. *ECS Solid State Lett.* **2013**, *2*, P28–P30. [CrossRef]
28. Jeong, Y.U.; Manthiram, A. Amorphous Tungsten Oxide/Ruthenium Oxide Composites for Electrochemical Capacitors. *J. Electrochem. Soc.* **2001**, *148*, A189–A193. [CrossRef]
29. Chen, K.Y.; Sun, Z.; Tseung, A.C.C. Preparation and Characterization of High-Performance Pt-Ru/WO_3-C Anode Catalysts for the Oxidation of Impure Hydrogen. *Electrochem. Solid-State Lett.* **2000**, *3*, 10–12. [CrossRef]
30. Yang, L.X.; Bock, C.; MacDougall, B.; Park, J. The role of the WO_x ad-component to Pt and PtRU catalysts in the electrochemical CH_3OH oxidation reaction. *J. Appl. Electrochem.* **2004**, *34*, 427–438. [CrossRef]
31. Ruzgas, T.; Csöregi, E.; Emnéus, J.; Gorton, L.; Marko-Varga, G. Peroxidase-modified electrodes: Fundamentals and application. *Anal. Chim. Acta* **1996**, *330*, 123–138. [CrossRef]
32. Ames, B.N.; Gold, L.S.; Willett, W.C. The causes and prevention of cancer. *Proc. Natl. Acad. Sci. USA* **1995**, *92*, 5258–5265. [CrossRef] [PubMed]
33. Kim, S.-J.; Kim, Y.L.; Yu, A.; Lee, J.; Lee, S.C.; Lee, C.; Kim, M.H.; Lee, Y. Electrospun iridium oxide nanofibers for direct selective electrochemical detection of ascorbic acid. *Sens. Actuators B* **2014**, *196*, 480–488. [CrossRef]
34. Park, J.; Lee, J.W.; Ye, B.U.; Chun, S.H.; Joo, S.H.; Park, H.; Lee, H.; Jeong, H.Y.; Kim, M.H.; Baik, J.M. Structural Evolution of Chemically-Driven RuO_2 Nanowires and 3-Dimensional Design for Photo-Catalytic Applications. *Sci. Rep.* **2015**, *5*, 11933. [CrossRef] [PubMed]
35. Habazaki, H.; Hayashi, Y.; Konno, H. Characterization of electrodeposited WO_3 films and its application to electrochemical wastewater treatment. *Electrochim. Acta* **2002**, *47*, 4181–4188. [CrossRef]
36. Shi, J.; Allara, D.L. Characterization of High-Temperature Reactions at the BaO/W Interface. *Langmuir* **1996**, *12*, 5099–5108. [CrossRef]
37. Morgan, D.J. Resolving ruthenium: XPS studies of common ruthenium materials. *Surf. Interface Anal.* **2015**, *47*, 1072–1079. [CrossRef]
38. Karlsson, R.K.B.; Cornell, A.; Pettersson, L.G.M. Structural Changes in RuO_2 during Electrochemical Hydrogen Evolution. *J. Phys. Chem. C* **2016**, *120*, 7094–7102. [CrossRef]
39. Zhang, W.; Tan, Y.; Gao, Y.; Wu, J.; Tang, B.; Zhao, J. Amorphous nickel–boron and nickel–manganese–boron alloy as electrochemical pseudocapacitor materials. *RSC Adv.* **2014**, *4*, 27800–27804. [CrossRef]
40. El-Kady, M.F.; Strong, V.; Dubin, S.; Kaner, R.B. Laser Scribing of High-Performance and Flexible Graphene-Based Electrochemical Capacitors. *Science* **2012**, *335*, 1326. [CrossRef]
41. Jo, A.; Kang, M.; Cha, A.; Jang, H.S.; Shim, J.H.; Lee, N.S.; Kim, M.H.; Lee, Y.; Lee, C. Nonenzymatic amperometric sensor for ascorbic acid based on hollow gold/ruthenium nanoshells. *Anal. Chim. Acta* **2014**, *819*, 94–101. [CrossRef] [PubMed]
42. Zare, H.R.; Chatraei, F. Preparation and electrochemical characteristics of electrodeposited acetaminophen on ruthenium oxide nanoparticles and its role as a sensor for simultaneous determination of ascorbic acid, dopamine and *N*-acetyl-l-cysteine. *Sens. Actuators B* **2011**, *160*, 1450–1457. [CrossRef]

43. Wu, J.; Suls, J.; Sansen, W. Amperometric determination of ascorbic acid on screen-printing ruthenium dioxide electrode. *Electrochem. Commun.* **2000**, *2*, 90–93. [CrossRef]
44. Prakash, P.; Wei Ting, S.; Chen, S.-M. Amperometric and Impedimetric H_2O_2 Biosensor Based on Horseradish Peroxidase Covalently Immobilized at Ruthenium Oxide Nanoparticles Modified Electrode. *Int. J. Electrochem. Sci.* **2011**, *6*, 2688–2709.
45. Anjalidevi, C.; Dharuman, V.; Shankara Narayanan, J. Non enzymatic hydrogen peroxide detection at ruthenium oxide–gold nano particle–Nafion modified electrode. *Sens. Actuators B* **2013**, *182*, 256–263. [CrossRef]